

Particle production during inflation: constraints expected from redshifted 21 cm observations from the epoch of reionization

Suvedha Suresh Naik,¹ Pravabati Chingangbam,^{2,3} Kazuyuki Furuuchi¹

¹Manipal Centre for Natural Sciences, Centre of Excellence, Manipal Academy of Higher Education, Dr. T.M.A. Pai Planetarium Building, Manipal 576 104, Karnataka, India

²Indian Institute of Astrophysics, Koramangala II Block, Bangalore 560 034, India

³School of Physics, Korea Institute for Advanced Study, 85 Hoegiro, Dongdaemun-gu, Seoul, 02455, Korea

E-mail: suvedha.nail@learner.manipal.edu, prava@iiap.res.in, kazuyuki.furuuchi@manipal.edu

Abstract. We examine a type of features in the primordial scalar power spectrum, namely, the bump-like feature(s) that arise as a result of burst(s) of particle production during inflation. The latest CMB observations by *Planck* 2018 can accommodate such features. In the near future, observations of redshifted 21 cm signal from the epoch of reionization can put additional constraints on inflation models by exploiting the expected tomographic information across a wide range of co-moving wave-numbers. In this work, we study the potential of upcoming observational data from SKA-Low to constrain the parameters of the primordial power spectrum with bump-like features. We use simulated mock data expected from SKA-Low, with uncertainties estimated from different foreground removal models, and constrain the parameters of primordial features within a Bayesian framework. We study two scenarios: in the first scenario where the astrophysical parameters relevant to the evolution of the 21 cm signal are known, we find that 21 cm power spectra do have the potential to probe the primordial bump-like features. As the input amplitude of the bump is decreased below roughly 10% of the amplitude of the primordial power spectrum without the bump, the uncertainties in the recovered values for both amplitude and location of the bump are found to increase, and the recovered values of the location of the bump also get increasingly more biased towards higher values. Hence, it becomes harder to constrain these parameters. In the second scenario, we analyze the achievable constraints on primordial features when two of the astrophysical parameters, namely, minimum halo mass and ionizing efficiency are uncertain. We find that the effect of the bump on the shape and the amplitude of the 21 cm power spectrum is distinct from the impact of varying the astrophysical parameters, and hence they may potentially be distinguished.

Contents

1	Introduction	1
2	Primordial features due to particle productions during inflation	3
3	Methodology	5
3.1	Redshifted 21 cm line as a probe of the early universe	6
3.1.1	Statistical tools - 21 cm global signal and power spectrum	7
3.2	Generating expected 21 cm power spectra	8
3.2.1	Redshifted 21 cm signal	8
3.2.2	Noise power spectra	8
3.3	MCMC sampling	9
3.3.1	Choice of priors	9
4	Results	11
4.1	Constraining the single bump model parameters keeping astrophysical parameters fixed	13
4.2	Constraining the parameters of single bump and EoR models simultaneously	15
5	Summary and discussions	16
A	Degeneracy between the single bump model parameters and the EoR parameters	19

1 Introduction

Inflation [1–6] is regarded as a standard framework for constructing theoretical models that can explain the fine-tuned initial conditions of the Big Bang model. The quantum fluctuations generated during inflation are considered as the origin of primordial density perturbations. These density fluctuations evolve in time and result in the structures that we observe in cosmological data. The observational data is then expected to contain imprints of the physics that operated during the primordial epoch.

During the last few decades, substantial effort has been made to probe primordial density perturbations using the Cosmic Microwave Background (CMB) anisotropies and fluctuations in the spatial distribution of galaxies. The current status is that the observations are consistent with the concordance Λ CDM model. In the concordance model, the primordial density fluctuations are described by a nearly scale-invariant primordial power spectrum. The CMB measurements from *Planck* [7, 8] have tightly constrained the parameters of the concordance Λ CDM model. However, the data contains larger uncertainties towards the large and small scales and can accommodate primordial power spectra that exhibit deviations from the nearly scale-invariant form. On the theoretical modelling side, the inflationary framework accommodates a variety of theoretical models which can be investigated by probing their unique signatures or “features” that manifest themselves as deviations from near scale-invariance

of the primordial power spectrum at different scales. Probing the primordial features using observations across a wide range of wave-numbers will further tighten the constraints on inflationary models.

A class of models involving bursts of particle production during inflation predicts bump-like features on the primordial power spectrum [9–12]. In inflation models based on higher dimensional gauge theories, such bursts of particle production may occur naturally [13–15] motivating the search for the signatures of bump-like features in cosmological observations. Recently, the presence of such features was investigated with the latest CMB data from the *Planck* satellite [16]. The *Planck* data puts constraints on the amplitude of the bump-like features on co-moving wave-numbers $0.0002 \lesssim k(\text{Mpc}^{-1}) \lesssim 0.15$, which in turn constrains the coupling parameter responsible for particle production during inflation. The bump-like features were also investigated with the galaxy two-point correlation functions [17], future CMB observations and galaxy surveys [18].

Neutral hydrogen, being the most abundant baryonic matter, has the potential to probe the unexplored windows of the universe via the 21 cm signal from its hyperfine transition [19–21]. The 21 cm fluctuations during the cosmic dawn are direct tracers of the underlying matter distribution and hence ideal for probing the primordial density fluctuations [22]. The upcoming redshifted 21 cm observations from instruments such as the Hydrogen Epoch of Reionization Array (HERA) [23] and Square Kilometre Array (SKA) [24] are expected to significantly improve our understanding of physics at different epochs of the universe. Extracting the signatures of primordial features from the future redshifted 21 cm signal will be challenging due to the uncertainty in astrophysical processes, foreground contamination and instrumental noise. However, the tomographic study of redshifted 21 cm signal provides the hope to probe the early universe when information from different statistical measures such as sky-averaged 21 cm signal, power spectrum and higher order correlators are combined. Previous studies have investigated prospects of probing the primordial universe with near-future redshifted 21 cm observations. In particular, the potential of the highly redshifted 21 cm signals to constrain the primordial oscillatory features was studied in [25]. The primordial features of resonant and step inflation models were investigated in [26] with the expected 21 cm intensity mapping observations by SKA1-Mid¹ and Tianlai observations [28]. The primordial features of kink, step and warp types were studied in [29] with intensity mapping from SKA1-Mid and the expected photometric surveys from LSST [30]. However, the studies [25, 26, 29] have used the Fisher information matrix to forecast the uncertainties of their model parameters. The Fisher matrix approach assumes ideal observations with the uncertainty containing the description of all sources of errors. Recently, the position of the absorption trough in the global 21 cm signal from the EDGES experiment [31] was used as a probe of the amplitude of the small-scale primordial power spectrum [32, 33]. To the best of our knowledge, a detailed analysis of the primordial features with more realistic observations from future 21 cm telescopes has not been carried out.

In this paper, we perform Bayesian analysis against the simulated data expected from near-future redshifted 21 cm observations to probe particle production during inflation. As the redshifted 21 cm observations are expected to probe the matter distribution across various co-moving wave-numbers, 21 cm surveys will provide information in addition to what is available from CMB and LSS. In particular, we study the signatures of bump-like features in the redshifted 21 cm signal from the Epoch of Reionization (EoR), targeted in SKA-

¹The SKA’s mid-frequency instrument covering 350 MHz to 14 GHz [27].

Low². We generate the uncertainty expected from SKA-Low by considering their antenna coordinates to mimic more realistic observations than what is obtained from Fisher matrix formalism. As the cosmic 21 cm signal is sensitive to initial conditions and the underlying astrophysical parameters at different redshifts, one needs a systematic exploration of these parameters. To obtain detailed information on the constrained parameters and degeneracies, we use the Markov Chain Monte Carlo (MCMC) approach to numerically evaluate the posterior probability distributions of the parameters. We examine the ability of SKA-Low to recover the parameters of primordial features within a Bayesian MCMC framework. We investigate the possibility of the existence of primordial features in the co-moving wave number range $0.1 \lesssim k(\text{Mpc}^{-1}) \lesssim 1.0$. We find that SKA-Low does have the potential to probe the presence of primordial features when the astrophysical parameters are fixed to their benchmark values considered in this work. We also discuss the challenges in recovering the parameters of primordial features in the case of uncertain astrophysical parameters.

This article is organized as follows: the primordial power spectrum motivated by particle production during inflation is briefly described in section 2. In section 3, we provide the methodology followed in this work. Mainly, this section describes the simulation of redshifted 21 cm signals, the generation of noise power spectrum from the SKA-Low and the details of MCMC sampling. In section 4, we present our results obtained from the Bayesian analysis. We summarize the study and discuss future directions in section 5.

2 Primordial features due to particle productions during inflation

The concordance model: Before discussing the primordial features investigated in this work, we provide the primordial power spectrum from the concordance Λ CDM model, which will be compared with the primordial power spectrum with features.

The concordance Λ CDM model assumes a scalar power spectrum parameterized by the amplitude of the scalar perturbations A_s and the scalar spectral index n_s :

$$P_s(k) = A_s \left(\frac{k}{k_0} \right)^{n_s - 1}, \quad (2.1)$$

where k is the co-moving wave-number and the pivot scale $k_0(\text{Mpc}^{-1})$ is chosen to be 0.05 [7].

Models with primordial features due to particle production during inflation: We study a class of inflation models [9–12] in which the inflaton field ϕ is coupled to a real scalar field χ through the interaction term

$$g^2(\phi - \phi_0)^2 \chi^2, \quad (2.2)$$

where g is the dimensionless coupling constant. When the inflaton field value crosses $\phi = \phi_0$, a burst of χ particle production occurs as they become instantaneously massless. When such an event occurs during the observable range of e -folds of inflation, it appears in the primordial power spectrum as a bump-like feature. Inflation models based on gauge theory in higher dimensions naturally give rise to the coupling of the form eq. (2.2) [13–15]. The coupling parameter g can be constrained by studying the imprints of bump-like features on cosmological observations.

²The SKA’s low-frequency instrument covering 50 to 350 MHz [27].

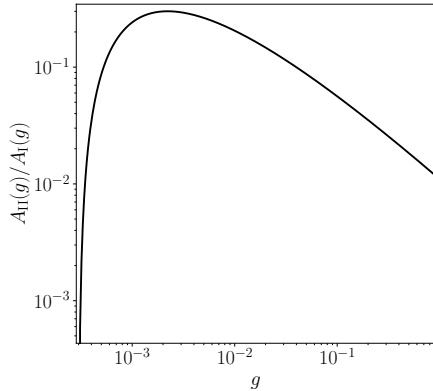


Figure 1: The ratio of the amplitudes of the subdominant feature A_{II} (eq. (2.7)) to the dominant feature A_I (eq. (2.6)) as a function of g .

We mention below the bounds on the coupling constant g as studied in [12]. The condition that the two-loop corrections are subdominant with respect to the leading one-loop contribution requires

$$g^2 \lesssim 3. \quad (2.3)$$

The condition that the mass of χ evolves quickly enough during the event of particle production requires

$$g^2 \gg 10^{-7}. \quad (2.4)$$

The primordial bump-like features produced due to particle production during inflation were fitted using numerical results in [10, 11]. In this work, we parameterize the primordial power spectrum by considering the latest analytical results [12]. The dominant and subdominant contributions to the power spectrum were calculated analytically with one-loop approximations and given by

$$P_s(k) = A_s \left(\frac{k}{k_0} \right)^{n_s-1} + A_I \sum_i \left(\frac{f_1(x_i)}{f_1^{\max}} \right) + A_{II} \sum_i \left(\frac{f_2(x_i)}{f_2^{\max}} \right), \quad (2.5)$$

where A_I and A_{II} are amplitudes of dominant and subdominant contributions, respectively. For an inflation model involving a coupling to a real scalar field as in eq. (2.2), the amplitudes depend on the model parameter g as³

$$A_I \simeq 6.6 \times 10^{-7} g^{7/2}, \quad (2.6)$$

$$A_{II} \simeq 1.1 \times 10^{-10} g^{5/2} \ln \left(\frac{g}{0.0003} \right)^2. \quad (2.7)$$

In figure 1, we plot the ratio of equations (2.6) and (2.7) as a function of the parameter g within the bounds given by (2.3) and (2.4).

³The dependence of A_I and A_{II} on g is the case of a real scalar field. A factor of two should be multiplied appropriately for the case of a complex scalar field. For models based on gauge theory in higher dimensions [13–15], the interaction of the form eq. (2.2) arises from the minimal coupling of a gauge field with a charged scalar field that is complex, with g being the 4D gauge coupling.

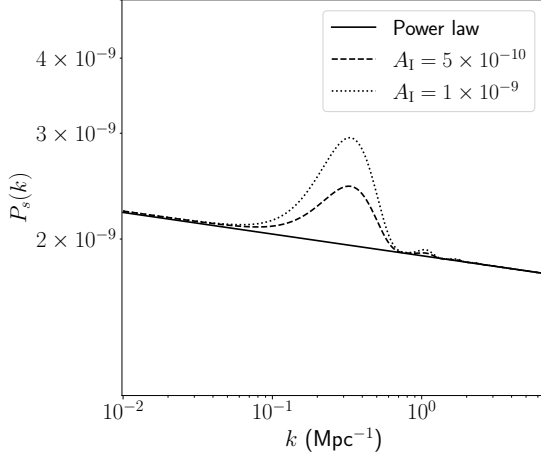


Figure 2: Single bump models with $k_b = 0.1(\text{Mpc}^{-1})$ (the peaks occur at $3.35 \times k_b$), and A_I set at 1.0×10^{-9} (dotted) and 5.0×10^{-10} (dashed). The primordial power spectrum for the power law is plotted in a solid line.

The scale dependence of the contributions are given by the dimensionless functions

$$f_1(x_i) \equiv \frac{[\sin(x_i) - \text{SinIntegral}(x_i)]^2}{x_i^3}, \quad (2.8)$$

$$f_2(x_i) \equiv \frac{-2x_i \cos(2x_i) + (1 - x_i^2) \sin(2x_i)}{x_i^3}, \quad (2.9)$$

where $x_i \equiv \frac{k}{k_i}$, and $\text{SinIntegral}(x) = \int_0^x \frac{\sin z}{z} dz$. The peaks of the functions $f_1(x)$ and $f_2(x)$ evaluate to $f_1^{\max} \simeq 0.11$ and $f_2^{\max} \simeq 0.85$, respectively. The parameter $k_i(\text{Mpc}^{-1})$ is related to the location of the i^{th} feature on the primordial power spectrum. The peak of the i^{th} dominant function occurs at

$$k_{p,i} \simeq 3.35 \times k_i, \quad (2.10)$$

and the subdominant function occurs at $x_i \simeq 1.25$.

In this work, we focus on a simple scenario of a single burst of particle production during inflation. The primordial power spectrum for a single bump having an amplitude A_I located at the scale k_b (i.e. the peak at $\sim 3.35 \times k_b(\text{Mpc}^{-1})$) is given by

$$P_s(k) = A_s \left(\frac{k}{k_0} \right)^{n_s-1} + A_I \left(\frac{f_1(k/k_b)}{f_1^{\max}} \right) + A_{II} \left(\frac{f_2(k/k_b)}{f_2^{\max}} \right). \quad (2.11)$$

The primordial power spectrum for a single bump model is shown in figure 2.

3 Methodology

This section describes our method for investigating the primordial bump-like features with the redshifted 21 cm line observations expected from SKA-Low.

3.1 Redshifted 21 cm line as a probe of the early universe

The redshifted 21 cm line can be a valuable probe of the high redshift universe, including the Epoch of Reionization (EoR) and the dark ages [19–22, 34]. The observable quantity is the differential brightness temperature at redshift z , which quantifies the change in brightness temperature induced by the 21 cm line emitted by a patch of neutral hydrogen relative to the background radiation and given by (e.g., [19, 35, 36])

$$\delta T_b(z) \simeq 9(1 + \delta_b)x_{\text{HI}}(1 + z)^{1/2} \left[1 - \frac{T_\gamma(z)}{T_S} \right] \left[\frac{H(z)/(1 + z)}{dv_{\parallel}/dr_{\parallel}} \right] \text{mK}, \quad (3.1)$$

where δ_b is the fractional baryon density perturbation, x_{HI} is the neutral fraction of hydrogen, $H(z)$ is the Hubble parameter and $dv_{\parallel}/dr_{\parallel}$ is the proper velocity gradient along the line of sight. The spin temperature T_S quantifies the relative number densities of atoms in the two hyperfine levels of the electronic ground state, and T_γ is the brightness temperature of the background radiation field, which is CMB in most cases. The quantity δ_b is the tracer of the total matter density, which is relevant for probing the primordial density fluctuations, and quantities x_{HI} and T_S are driven by the astrophysical processes that model the formation of the first ionizing sources and reionization of the universe.

We use 21cmFAST [37, 38], a semi-numerical simulation code, to simulate the cosmological 21 cm signal. 21cmFAST generates realizations of the density, ionization, spin-temperature fields, and velocity gradient, which can be combined to give the 21 cm brightness temperature field using eq. (3.1). We work in the framework of Friedmann-Lemaître-Robertson-Walker cosmology with a flat spatial geometry. The concordance Λ CDM model is parametrized by the baryon density $\omega_b = \Omega_b h^2$, the cold dark matter density $\omega_{\text{cdm}} = \Omega_{\text{cdm}} h^2$, the present Hubble parameter H_0 , the optical depth to reionization τ , the amplitude of the scalar perturbations A_s at the pivot scale $k_0 = 0.05(\text{Mpc}^{-1})$ (or σ_8 , the variance of the density fluctuations within a sphere of $8h^{-1}\text{Mpc}$ radius) and the spectral index n_s . The brightness temperature of the 21 cm line is sensitive to the underlying astrophysical processes, which in the simulations are modelled as being parametrized by some variables. Some of the important parameters are:

- M_{min} - the halo mass below which the abundance of active star-forming galaxies is exponentially suppressed
- f_{esc} - the normalization of the ionizing UV escape fraction of high- z galaxies
- f_* - the fraction of galactic gas in stars
- α_* - the power-law scaling of f_* with halo mass
- α_{esc} - the power-law scaling of f_{esc} with halo mass
- t_* - the star formation time-scale taken as a fraction of the Hubble time
- E_0 - the minimum X-ray photon energy capable of escaping the galaxy and
- $L_{X < 2\text{keV}}/\text{SFR}$ - the normalization of the soft-band X-ray luminosity per unit star formation, computed over the band 2 KeV.

The astrophysical parameters are extremely uncertain at high redshifts. Therefore, MCMC sampling of all uncertain parameters is required when the actual data arrive. However, simultaneous variation of all the parameters becomes computationally expensive, particularly when the initial conditions need to be generated every time to sample the cosmological parameters.

To perform the analysis in a reasonable computational time, we choose two of the astrophysical parameters that are important for EoR modelling. The first is M_{\min} (in solar mass units M_{\odot}), which can be expressed in terms of the virial temperature T_{vir} (K) as [36]

$$M_{\min} = 10^8 h^{-1} \left(\frac{\mu}{0.6} \right)^{-3/2} \left(\frac{\Omega_m}{\Omega_m^z} \frac{\Delta_c^z}{18\pi^2} \right)^{-1/2} \left(\frac{T_{\text{vir}}}{1.98 \times 10^4 \text{K}} \right)^{3/2} \left(\frac{1+z}{10} \right)^{-3/2} M_{\odot}, \quad (3.2)$$

where μ is the mean molecular weight, $\Omega_m^z = \Omega_m(1+z)^3/[\Omega_m(1+z)^3 + \Omega_{\Lambda}]$, and $\Delta_c^z = 18\pi^2 + 82d^z - 39d^{z^2}$, where $d^z = \Omega_m^z - 1$. The second is the UV ionizing efficiency of high- z galaxies ζ , which is modelled as

$$\zeta = 30 \left(\frac{f_{\text{esc}}}{0.12} \right) \left(\frac{f_*}{0.05} \right) \left(\frac{N_{\gamma}}{4000} \right) \left(\frac{1.5}{1+n_{\text{rec}}} \right), \quad (3.3)$$

where N_{γ} is the number of ionizing photons produced per baryons in stars and n_{rec} is the typical number of times a hydrogen atom recombines. For high- z galaxies, the parameters f_{esc} and f_* are very uncertain. Keeping in mind a reasonable computational time for the analysis, we consider the product of eq (3.3) as a free parameter rather than varying each of them individually. To account for the inaccuracy of semi-numerical simulations, we add a modelling uncertainty of 20% in our analysis (see also section 3.3).

We fix our *fiducial model* as follows: the cosmological parameters are set following the best-fit values of *Planck* 2018 results [8]⁴: $\Omega_b h^2 = 0.022$, $\Omega_{\text{cdm}} h^2 = 0.120$, $h = 0.6736$, $\tau = 0.054$, $\sigma_8 = 0.811$ and $n_s = 0.965$. We fix the astrophysical parameters following [39]: $M_{\min} = 5 \times 10^8 M_{\odot}$ or $\log T_{\text{vir}} = 4.69897$, $\zeta = 30$ (i.e., $f_{\text{esc}} = 0.1$, $f_* = 0.05$ and $N_{\gamma} = 5000$), $\alpha_* = 0.5$, $\alpha_{\text{esc}} = -0.5$, $t_* = 0.5$, $E_0 = 0.5$ KeV and $L_{X<2\text{KeV}}/\text{SFR} = 10^{40.5}$ erg s⁻¹ M_{\odot}^{-1} yr.

In this work, we introduce the additional parameters of the bump-like features of the primordial power spectrum described in section 2. In 21cmFAST, the primordial power spectrum is calculated using the default power-law form [40, 41], which we modify according to eq. (2.11). We first study the impact of primordial features on the differential brightness temperature while keeping the astrophysical parameters fixed to their fiducial values. Next, we allow T_{vir} and ζ to vary along with the parameters of primordial features and carry out joint parameter estimation.

3.1.1 Statistical tools - 21 cm global signal and power spectrum

The redshifted 21 cm observations provide three-dimensional information on the neutral hydrogen distribution in the universe. In order to extract physical information from the data, we can use different statistical tools.

The simplest tool is the sky-averaged global 21 cm signal, denoted by $\delta\bar{T}_b$. We will discuss how the global 21 cm signal can constrain the amplitude of the primordial power spectrum in section 3.3.1. Since the global 21 cm signal is averaged over the entire sky, we lose the information in the spatial fluctuations of the signal. To extract information from the fluctuations, the most commonly used statistic is the power spectrum $P_{21}(k)$ given by

$$\langle \delta_{21}(\vec{k}) \delta_{21}^*(\vec{k}') \rangle = (2\pi)^3 \delta_D^{(3)}(\vec{k} - \vec{k}') P_{21}(k), \quad (3.4)$$

where $\langle \dots \rangle$ denotes the ensemble average, $\delta_{21}(\vec{k})$ is the Fourier transform of the quantity $\delta_{21}(\vec{x}) \equiv [\delta T_b(\vec{x}) - \delta\bar{T}_b]/\delta\bar{T}_b$ and $\delta_D^{(3)}(\vec{k})$ is the 3D Dirac delta function. $P_{21}(k)$ is a function

⁴The best-fit values obtained with the combination of temperature, polarization and lensing data.

of only the magnitude of the wave-number k due to the assumption of homogeneity and isotropy.

The 21 cm power spectrum is sensitive to underlying astrophysical processes at different redshifts via eq. (3.1). Ideally, the imprints of primordial features are more prominent in the 21 cm power spectrum at high redshifts where fluctuations in x_{HI} and T_{S} are negligible. However, observations at such high redshifts become extremely challenging as the radio sky at low frequency is dominated by the foreground emission. In our MCMC sampling, we use the simulated 21 cm power spectra after the formation of the first stars until the end of reionization to probe the imprints of primordial features.

3.2 Generating expected 21 cm power spectra

Observations of 21 cm power spectra will contain the cosmological 21 cm signal and the noise component given by

$$P_{21}^{\text{obs}}(k) = P_{21}^{\text{signal}}(k) + P_{21}^{\text{noise}}(k), \quad (3.5)$$

where $P_{21}^{\text{signal}}(k)$ is the power spectrum of cosmological redshifted 21 cm signal without foreground emission and $P_{21}^{\text{noise}}(k)$ is the noise power spectrum expected from SKA-Low. In this section, we describe the generation of both these components to use the combined power spectrum as ‘mock’ observations.

3.2.1 Redshifted 21 cm signal

The simulation parameters relevant for generating the redshifted 21 cm signal in 21cmFAST are the length of the simulation box L , and the number of cells on each side of the simulation box N . The parameters L and N set the minimum and maximum wave-numbers simulated by 21cmFAST, respectively. Typically, a large simulation box size ($L \geq 250$ Mpc) is required to simulate cosmic dawn and EoR power spectra⁵. We choose a box length of 600 Mpc, starting from a higher resolution box with the number of cells 600, sampling down to a lower-resolution box with the number of cells 200. Such a simulation gives a resolution of 3 Mpc. We simulate the 21 cm power spectra at various redshifts in the range $6 \lesssim z \lesssim 20$ ⁶.

The input values of the parameters A_{I} , k_b , ζ and T_{vir} , chosen to create the mock observations, are mentioned in section 4 with their results.

3.2.2 Noise power spectra

The sensitivity of an interferometer to the 21 cm signal depends on the thermal noise in the interferometric visibilities and the sample variance calculated from the number of independent modes measured by the interferometer.

We generate the noise power spectra expected from the upcoming telescope SKA-Low [24] using the package 21cmSense [43–45]. SKA-Low will operate in the frequency range $50 \lesssim \nu(\text{MHz}) \lesssim 350$ and is expected to probe the universe in its early stage with an order of magnitude better sensitivity than the currently operating radio telescopes. The antenna parameters for SKA-Low are given in table 1. The ‘core’ of SKA-Low consists of short-baseline antennas, which are useful for sensitivity calculations [27]. The antenna coordinates in latitude and longitude are available on the SKA page [46].

⁵Box length $L < 250$ Mpc underestimates the large-scale power during the cosmic dawn by 7–9% on average [42].

⁶In principle, 21 cm signals from higher redshifts are more sensitive to primordial density perturbations (see appendix A), however, the corresponding lower frequencies are more strongly dominated by Galactic foreground (mainly synchrotron) emissions. Our choice of redshift range gives a compromise between the two.

Parameters	Values
Number of antennae in the core	224
Element size [m]	38
Latitude	26°49'29"S
Longitude	116°45'52"E
Receiver temperature [K]	100
Total observation time [hr]	1080

Table 1: SKA-Low specifications used for producing the noise power spectra.

The power spectrum of the thermal noise for a single baseline is given by [47]

$$\Delta_{\text{noise}}^2(k) \approx X^2 Y \frac{k^3}{2\pi^2} \frac{\Omega}{2t} T_{\text{sys}}^2, \quad (3.6)$$

where X converts angles on the sky to transverse distances, Y converts from bandwidth to line-of-sight distance, $\Omega(\text{sr})$ is the solid angle of the primary beam of one element, T_{sys} gives the system temperature, and the integration time is given by t . The system temperature has two parts: the sky and the receiver temperature, i.e., $T_{\text{sys}} = T_{\text{sky}} + T_{\text{rec}}$. The receiver temperature is set at 100 K, and the sky temperature is modelled as [48]

$$T_{\text{sky}} = 60\text{K} \left(\frac{300 \text{ MHz}}{\nu} \right)^{2.55}. \quad (3.7)$$

The sensitivity estimated in `21cmSense` depends on how the foreground wedge is accounted for while calculating the noise. The ‘moderate’ foreground removal model assumes a foreground wedge that extends $0.1 h(\text{Mpc}^{-1})$, and the ‘optimistic’ foreground removal model assumes a foreground wedge extending to the primary field of view [44].

3.3 MCMC sampling

We use `21CMMC` [49–51], which efficiently samples the parameter space within a Bayesian MCMC framework based on the `EMCEE PYTHON` module [52]. `21CMMC` uses a modified version of `21cmFAST` to reduce computational time. We add the analytical power spectrum template given by (2.11) in the initial conditions of `21CMMC`. To vary cosmological parameters in `21CMMC`, every time the sampler proposes a new parameter position, the initial conditions need to be generated with a different random seed which becomes computationally expensive. Therefore, we chose the length of the simulation box to be 250 Mpc and a resolution of 3 Mpc (the same as mock observations) for the sampled simulations to have a reasonable computational time and reasonable accuracy when compared to the mock observations of higher box lengths. In `21CMMC`, sampling is performed in the region $0.1 \lesssim k(\text{Mpc}^{-1}) \lesssim 1^7$. In addition to the uncertainties from instrument and sample variance, a modelling uncertainty of 20% is included to account for the inaccuracy of semi-numerical approaches [39, 50].

3.3.1 Choice of priors

The single bump model is parameterized by the amplitude of the bump A_I and the location of the bump $k_b(\text{Mpc}^{-1})$. We choose uniform prior probability for both parameters in the Bayesian analysis. The choices of upper and lower bounds are described in the following.

⁷The lower bound accounts for foreground domination in the moderate foreground removal model, and the upper bound accounts for shot-noise domination [49].

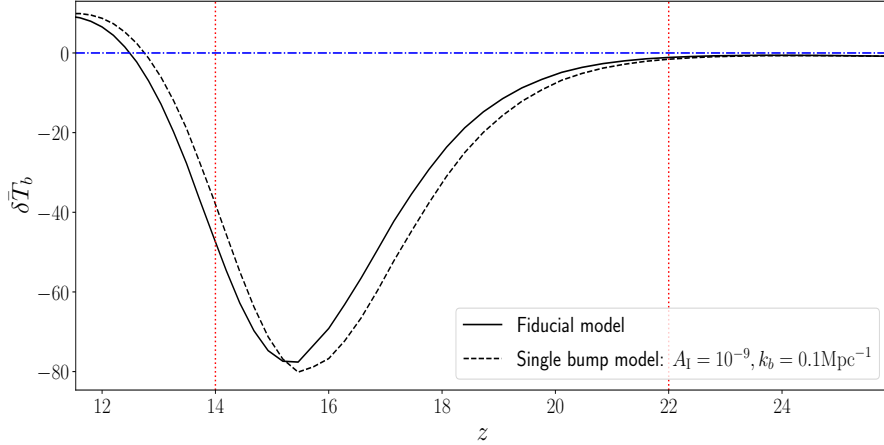


Figure 3: The global 21 cm signals expected for the fiducial and single bump models. The vertical lines indicate the region where the claimed absorption trough of the global 21 cm signal by EDGES [31] lies.

Amplitude of the bump: The theoretically estimated upper bound on the coupling parameter is given by eq. (2.3) which puts an upper bound on the amplitude via eq. (2.6) and is given by $A_I \lesssim 10^{-6}$. However, a bump-like feature located in the sampling region $[0.1, 1] \text{ Mpc}^{-1}$ and amplitude $A_I > A_s$ increases the power in the lower- k region due to the shape of the feature and affects the parameter σ_8 or the variance of density fluctuations. We consider an upper bound on A_I to be 10^{-9} so that the value of σ_8 is consistent with *Planck* 2018 constraints. The lower bound on g^2 calculated in [12] is given by eq. (2.4), which gives $A_I > 10^{-17}$. We first examine constraints on A_I based on already available 21 cm observations. The global 21 cm signal for the fiducial model is plotted in figure 3, along with the expected signal for the single bump model. The vertical lines indicate the region where the absorption trough of the global 21 cm signal obtained by the EDGES experiment [31] lies. Various groups have critically examined the EDGES results, and one of the recent results from [53] rejected the best-fit profile found by [31] with a 95.3% confidence level. Figure 3 shows that when the amplitude of the primordial power spectrum is increased by incorporating a primordial feature, the global 21 cm profile shifts towards the higher redshift. The reason for this shift is that the amplitude of the primordial fluctuations at small-scales affects structure formation, further affecting the timing when the Lyman- α sources are produced and thereby changing the redshift evolution of the global 21 cm signal [32, 33]. The constraints on A_I are weaker even if we take the EDGES observations into account.

We also investigate the possible constraints from published upper limits on 21 cm power spectra. In figure 4, we plot 21 cm power spectra in the following form

$$\Delta_{21}^2(k) := \left(\frac{k^3}{2\pi^2} \right) P_{21}(k). \quad (3.8)$$

The observational upper limits plotted are from facilities such as GMRT [54], LOFAR [55–57], MWA [58–66], PAPER [67], OVRO-LWA [68, 69], AARTFAAC [70] and HERA [71, 72]. The colour associated with each data point is given by the k value shown in the colour bar. For comparison with the expected 21 cm power spectra from single bump models, we also plot

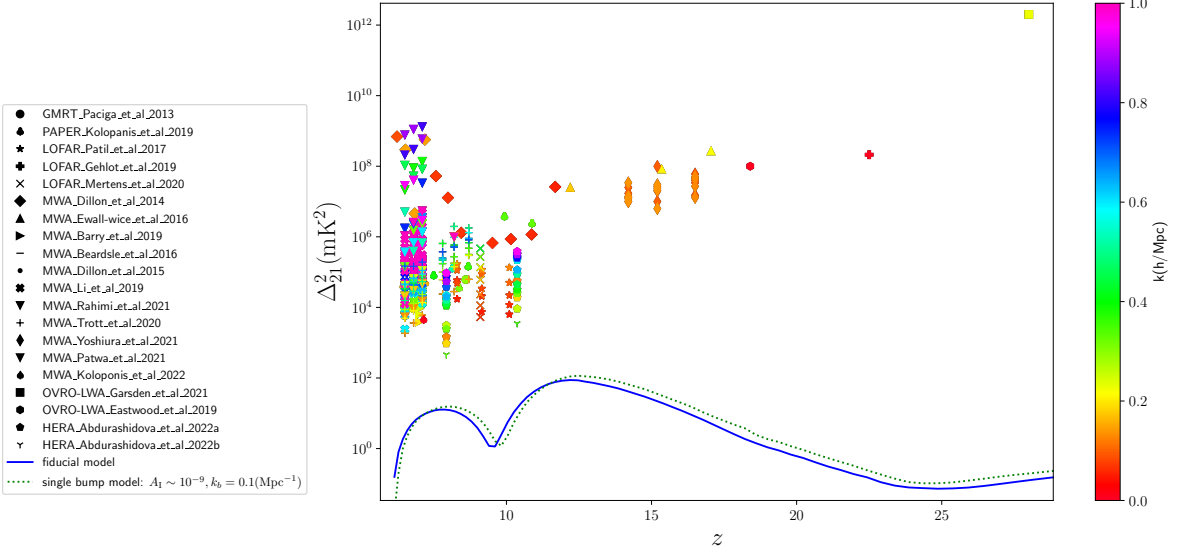


Figure 4: The upper limits on 21 cm power spectra from recent observations are shown with different markers. The colour bar gives the co-moving wave-number k in ($h\text{Mpc}^{-1}$) units. The simulated 21 cm power spectra for the fiducial and single bump model ($A_{\text{I}} = 10^{-9}$, $k_b = 0.1(\text{Mpc}^{-1})$ or $k_p \simeq 0.335(\text{Mpc}^{-1})$) are plotted in solid and dotted curves, respectively. The evolution of the simulated power spectra is shown at $k = 0.33(\text{Mpc}^{-1})$.

the redshift evolution of the corresponding 21 cm power spectra at $k = k_p = 0.33(\text{Mpc}^{-1})$ (the bump was introduced at $k_b = 0.1(\text{Mpc}^{-1})$). Figure 4 shows that the current upper limits are a few orders of magnitude greater than the simulated 21 cm power spectra for the fiducial and single bump models.

Following the above arguments, we choose an upper bound on the prior of A_{I} to be 10^{-9} . The lower bound on A_{I} is set to be 10^{-11} to have a distinguishable effect on the 21 cm power spectra. We assume a uniform prior probability distribution on $\log A_{\text{I}}$.

Location of the bump: A bump-like feature at location k_b on the primordial power spectrum peaks at a higher- k value given by eq. (2.10). We note that the parameter k_b is not restricted from the theoretical models. In order to make the peak of the bump appear in the co-moving wave-number range $[0.1, 1] \text{ Mpc}^{-1}$, we choose a uniform prior probability for k_b in the limits $[0.0299, 0.299] \text{ Mpc}^{-1}$.

4 Results

This section describes the constraints on primordial bump-like features expected with near-future observations of 21 cm power spectrum from SKA-Low.

We investigate the case of a single burst of particle production during inflation that predicts a single bump-like feature on the primordial power spectrum given by eq. (2.11). We first consider a scenario where we fix all the astrophysical parameters to their fiducial values as mentioned in section 3.1, and vary only the single bump model parameters in the MCMC sampling. We then discuss a scenario with the simultaneous variation of astrophysical and single bump model parameters.

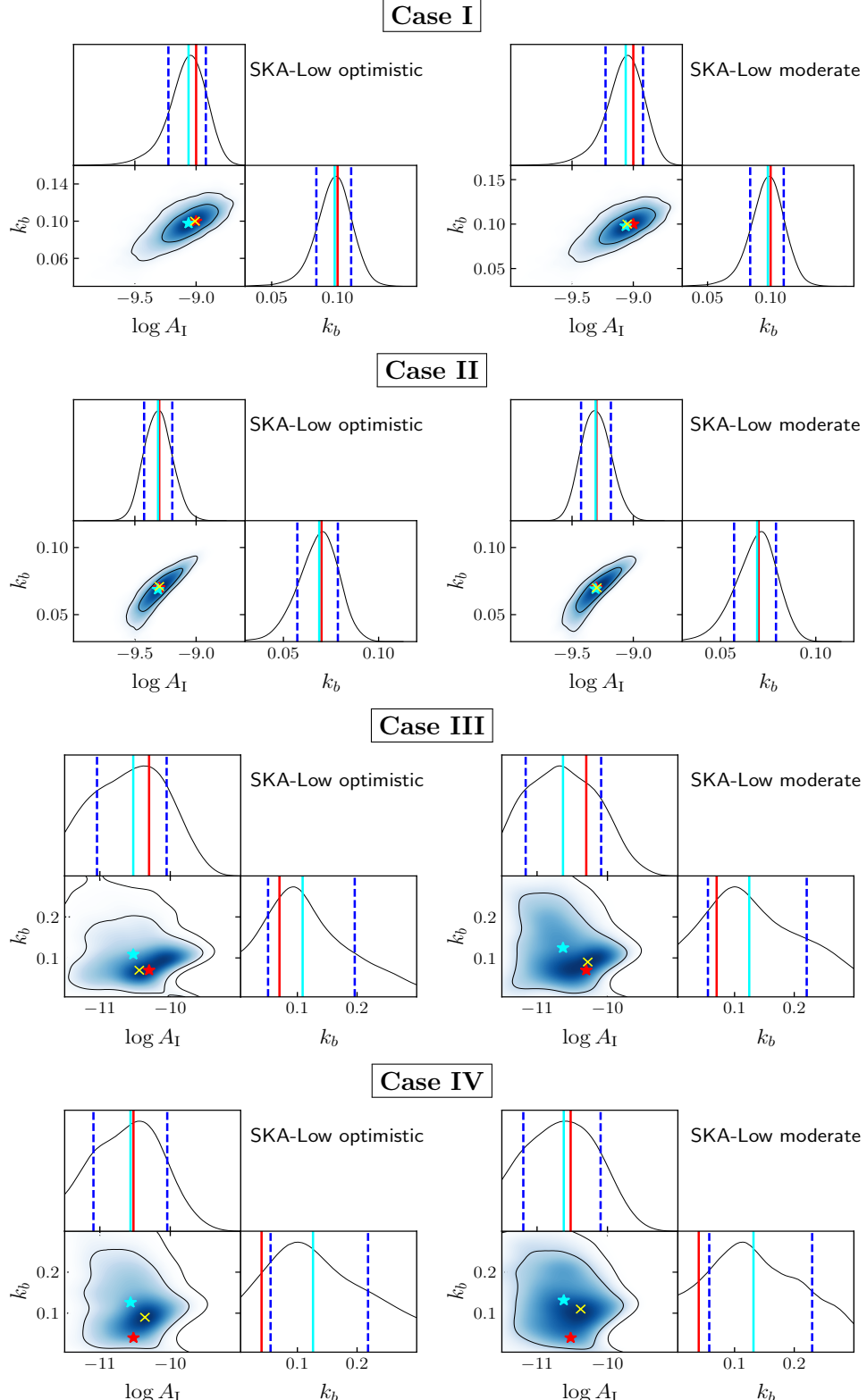


Figure 5: Posterior PDFs for the single bump model parameters $\log A_I$ and k_b using the sensitivity from SKA-Low with optimistic (left) and moderate (right) foreground removal models. The two contours indicate the parameter space corresponding to 68% and 95% CL, respectively. The red (cyan) star and lines mark the input parameter values (recovered median values from one-dimensional PDFs) (table 2). The vertical dashed lines indicate 68% parameter space enclosed in one-dimensional PDFs. The markers ‘ \times ’ denote the maxima for each two-dimensional PDF.

Parameters	Single bump models									
	Case I				Case II					
	Input	Optimistic		Moderate		Input	Optimistic		Moderate	
		Median	$\delta_\theta(\%)$	Median	$\delta_\theta(\%)$		Median	$\delta_\theta(\%)$	Median	$\delta_\theta(\%)$
$\log A_I$	-9.0	$-9.0619^{+0.1413}_{-0.1645}$	1.68	$-9.0620^{+0.1414}_{-0.1646}$	1.68	-9.3010	$-9.3110^{+0.1165}_{-0.1134}$	1.23	$-9.3077^{+0.1248}_{-0.1185}$	1.31
$k_b(\text{Mpc}^{-1})$	0.1	$0.0978^{+0.0125}_{-0.0139}$	13.49	$0.0978^{+0.0126}_{-0.0140}$	13.59	0.07	$0.0688^{+0.0098}_{-0.0115}$	15.48	$0.0692^{+0.0099}_{-0.0121}$	15.89
Parameters	Case III				Case IV					
	Input	Optimistic		Moderate		Input	Optimistic		Moderate	
		Median	$\delta_\theta(\%)$	Median	$\delta_\theta(\%)$		Median	$\delta_\theta(\%)$	Median	$\delta_\theta(\%)$
$\log A_I$	-10.3010	$-10.5259^{+0.5220}_{-0.5260}$	4.97	$-10.6314^{+0.5418}_{-0.5301}$	5.04	-10.5228	$-10.5650^{+0.5420}_{-0.5460}$	5.14	$-10.6240^{+0.5232}_{-0.5746}$	5.16
$k_b(\text{Mpc}^{-1})$	0.07	$0.1088^{+0.0873}_{-0.0579}$	66.72	$0.1246^{+0.0963}_{-0.0692}$	66.41	0.04	$0.1262^{+0.0922}_{-0.0711}$	64.69	$0.1262^{+0.0963}_{-0.0741}$	67.51

Table 2: The results of single bump models investigated. For each case, we quote the input values used to produce the noise power spectra, the recovered median values from one-dimensional marginalized PDFs (with 68% CL) from SKA-Low and fractional uncertainties as given in eq. (4.1).

4.1 Constraining the single bump model parameters keeping astrophysical parameters fixed

To generate mock 21 cm power spectra, we follow the methodology described in section 3.2. We choose various input values of the single bump model parameters to produce mock power spectra and investigate the ability of SKA-Low to constrain them.

Case I: We first consider a single bump model with $A_I = 10^{-9}$, or about 50% of A_s and $k_b = 0.1(\text{Mpc}^{-1})$, which peaks at $k_p \sim 0.33(\text{Mpc}^{-1})$. We use both optimistic and moderate foreground removal model scenarios with 20% modelling uncertainty added to the noise power spectra. Table 2 provides the input values used to produce the noise power spectra and the recovered median values of the parameters obtained from the one-dimensional marginalized Probability Distribution Functions (PDF) with a 68% Confidence Level (CL). We also quote the fractional uncertainty on each recovered parameter θ having uncertainty σ_θ (68% CL) as

$$\delta_\theta := \frac{\sigma_\theta}{\theta}. \quad (4.1)$$

The two-dimensional posterior PDFs with the marginalized one-dimensional PDFs of single bump model parameters are plotted in the top row of figure 5⁸. Our results indicate that a primordial bump-like feature with parameters $A_I \sim 0.5A_s$ and $k_b = 0.1(\text{Mpc}^{-1})$ are recoverable within 68% CL using the SKA-Low configurations with an optimistic foreground removal model. We also carry out this analysis with a moderate foreground removal model, and the changes in the recovered values with their uncertainties are negligible, as reported in table 2.

Case II: Next, we test the detectability of a primordial bump-like feature with a smaller amplitude than the one mentioned above. Since the thermal uncertainties estimated from SKA-Low are less at lower- k values ($k < 0.3(\text{Mpc}^{-1})$) as in eq. (3.6), we create mock power spectra for a single bump model with the following parameter values: $A_I = 5 \times 10^{-10}$, or about 25% of A_s and $k_b = 0.07(\text{Mpc}^{-1})$, or $k_p \simeq 0.23(\text{Mpc}^{-1})$. We carry out MCMC sampling for the single bump case using the noise power spectra produced with both the moderate and

⁸The triangle plots of posterior PDFs are generated with the package `GetDist` [73].

optimistic foreground removal models. In both cases, 20% modelling uncertainty is added to the noise power, like in the previous case. Our results are given in table 2. The one- and two-dimensional PDFs of the parameters are shown in the second row of figure 5, which clearly indicates recovery of both parameters within 68% CL. Compared with the optimistic case, the moderate foreground removal model increases the fractional errors δ_θ (eq. (4.1)) on $\log A_I$ and k_b by 0.08% and 0.4%, respectively. We emphasize that even for the moderate foreground removal scenario, the parameters of the single bump model are recovered within 68% CL.

Case III: To test the recoverability of the lowest amplitude of the bump-like feature, we perform another MCMC sampling with an order of magnitude smaller amplitude than the previous case and k_b being the same as the previous case, i.e., $A_I = 5 \times 10^{-11}$ (or about 2.5% of A_s) and $k_b = 0.07(\text{Mpc}^{-1})$. The input values of the parameters with their recovered values are given in table 2. The corresponding one- and two-dimensional marginalized posterior distributions are shown in the third row of figure 5. Compared to the previous case in which bump-like features at the same k_b with an order of magnitude larger A_I , we found that the fractional errors on $\log A_I$ and k_b have increased by about 4% and 51%, respectively. Though the result indicates recovery of parameters within 68% CL, the posterior PDFs show that the primordial bump-like features of smaller amplitudes have wider PDFs with large uncertainties. The median values from the one-dimensional marginalized distributions are away from the input values due to their asymmetric PDFs. However, note that the values corresponding to the maxima of 2D PDFs ($(\log A_I, k_b)_{2D} = (-10.44, 0.076)$ for the optimistic case and $(\log A_I, k_b)_{2D} = (-10.28, 0.09)$ for the moderate case, marked with ‘ \times ’ in the figure) are close to the input values, as seen in the two-dimensional PDFs.

Case IV: In the current work, MCMC sampling is being performed in the wave-number range $0.1 \lesssim k(\text{Mpc}^{-1}) \lesssim 1$. In [16], the wave-number range $0.0002 \lesssim k(\text{Mpc}^{-1}) \lesssim 0.15$ was used to obtain upper bounds on A_I (95% CL) using the *Planck* 2018 data. The two ranges have a small overlap region, and the question arises whether SKA-Low can recover the bump-like feature that was allowed by CMB data. With this motivation, we choose $A_I = 3 \times 10^{-11}$ and $k_b = 0.04(\text{Mpc}^{-1})$ so that the peak of the bump appears at $k_p \simeq 0.13(\text{Mpc}^{-1})$. The results are provided in table 2. The one- and two-dimensional PDFs are shown in the bottom row of figure 5. The PDFs indicate that the median of A_I is close to the mock value chosen and recovered within 68% CL. However, k_b is recovered, not within 68%, but within 95% CL. We conclude that as the amplitude of the feature decreases, constraining k_b becomes more difficult with only a two-point correlation function.

We summarize the results of all the above cases in figure 6, which capture the trend of the parameter estimation, and the variation of the uncertainties as the true value of A_I is made smaller. We reiterate the important points that can also be discerned visually from this figure. First, the errors increase mildly from the optimistic to the moderate foreground removal scenario. Secondly, the errors do not scale monotonously with the input parameter values. Case II, which has input values of both parameters smaller than Case I, has marginally smaller errors, and the bias of the recovered versus input parameters values is also smaller. Thirdly, as we decrease A_I further, the errors increase, and the recovered median values of A_I show mild bias (within 68% CL) towards the lower side, while the recovered median k_b values show relatively stronger bias (beyond 68% CL) towards the higher side. The bias becomes stronger as the input value of A_I is decreased. This trend implies that k_b becomes harder to constrain.

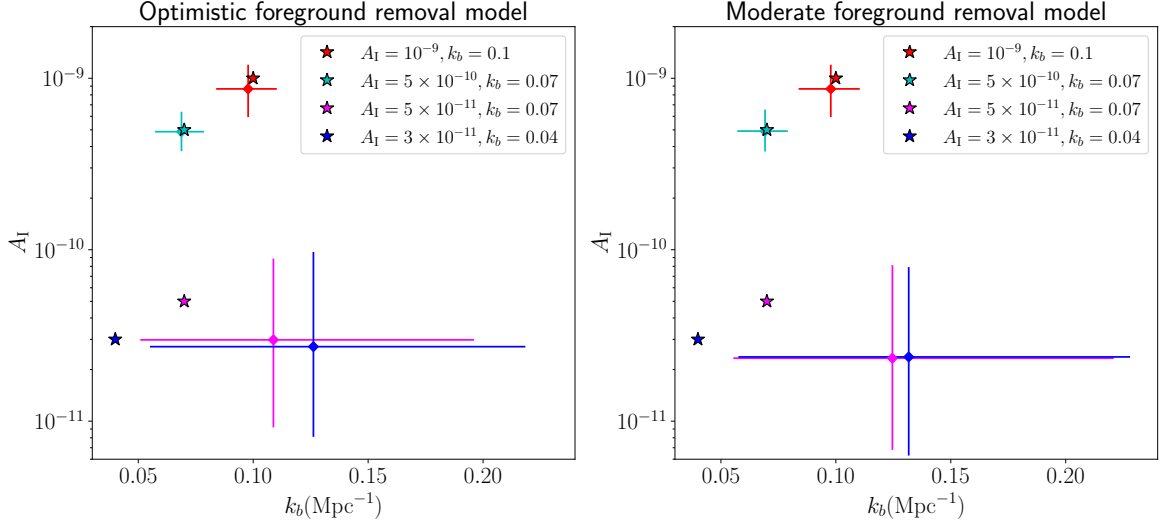


Figure 6: The median values of A_I and k_b with 68% CL uncertainties obtained from the analysis of single bump models with optimistic (left) and moderate (right) foreground removal models. The input values are represented with stars. Colour represents the model investigated.

Parameters	Input	Recovered values from SKA-Low	
		Median	δ_θ (%)
ζ	30	$30.3317^{+1.4173}_{-1.4583}$	4.74
$\log T_{\text{vir}}$	4.69897	$4.8319^{+0.0278}_{-0.0665}$	0.97
$\log A_I$	-9.3010	$-10.1103^{+0.6024}_{-0.5262}$	5.58
$k_b(\text{Mpc}^{-1})$	0.07	$0.0972^{+0.1027}_{-0.0370}$	71.86

Table 3: The results for the simultaneous constraining of the EoR and single bump model parameters. We quote the input values used to produce the noise power spectra, the recovered median values (with 68% CL) from one-dimensional marginalized distributions with SKA-Low sensitivity and the fractional uncertainties as given in eq. (4.1).

The above results are obtained by fixing the astrophysical parameters to their fiducial values and assuming 20% uncertainty associated with the semi-numerical modelling approach. In the subsequent section, we also vary two of the astrophysical parameters.

4.2 Constraining the parameters of single bump and EoR models simultaneously

As mentioned in section 3.1, the astrophysical parameters play a significant role in modelling the timing of the formation of the first luminous sources, heating of the IGM, and reionization of the universe. We consider a minimal model for reionization parameterized by the log of the virial temperature T_{vir} (K) i.e., $\log T_{\text{vir}}$ and the ionizing efficiency ζ . A uniform prior range for $\log T_{\text{vir}}$ was assumed in 21CMMC is [4, 6]. The lower limit is motivated by the minimum temperature for efficient atomic line cooling, and the upper limit is consistent with

the host halo masses of observed galaxies at $z \sim 6 - 8$ [50]. A uniform prior range of [10, 250] was chosen for ζ following [50] to explore the models where bright, rare galaxies drive reionization. For generating the mock data, we choose the values $\log T_{\text{vir}} = 4.69897$, consistent with $M_{\text{min}} = 5 \times 10^8 M_{\odot}$ (following eq. (3.2)), and $\zeta = 30$.

Note on degeneracy: A higher value of the parameter ζ corresponds to more efficient production of ionizing photons and results in earlier reionization. Similarly, a lower value of T_{vir} results in earlier reionization as more galaxies can form stars [19]. As discussed in section 3.3.1, the presence of a bump in the primordial power spectrum may affect structure formation and consequently change the timings of the epoch of heating and reionization. Therefore, degeneracy between these three parameters - T_{vir} , ζ and A_{I} , is expected. In appendix A, we include a discussion on the effect of the bump-like feature on the shape and amplitude of the 21 cm power spectrum and a comparison with the effect of varying the astrophysical parameters. We show that the effects are distinct from each other.

We now simultaneously constrain the EoR parameters ζ and T_{vir} and single bump model parameters A_{I} and k_b . The uncertainties we present are from the SKA-Low (optimistic foreground removal model) combined with 20% modelling uncertainty. Table 3 shows the parameters, their input values used in creating mock data, and the recovered median values from one-dimensional marginalized posterior PDF. In figure 7, we show the one- and two-dimensional posterior PDFs of all the parameters. Our results indicate that the input parameters are recovered in the following way: ζ and k_b within 68% CL, and $\log T_{\text{vir}}$ and $\log A_{\text{I}}$ within 95% CL. We can observe that the one-dimensional PDFs of all the parameters, except for ζ , deviate strongly from the Gaussian shape. This reflects the degeneracy among the parameters, which is quite evident from the two-dimensional PDFs. It is worth mentioning that the parameter values corresponding to a maximum in the two-dimensional PDF for $\log A_{\text{I}} - k_b$ ($(\log A_{\text{I}}, k_b)_{\text{2D}} = (-9.41, 0.076)$) are close to the input values compared to the recovered median values.

When we compare the results obtained here with the results for fixed ζ and T_{vir} (Case II, optimistic), we find that keeping ζ and T_{vir} as free parameters increases the fractional errors δ_{θ} (eq. (4.1)) on $\log A_{\text{I}}$ by 4% and k_b by 56%. The analysis with a moderate foreground removal model gives similar results as the optimistic case, and the difference in fractional errors of all four parameters is less than 2%.

5 Summary and discussions

In this work, we studied the potential of upcoming redshifted 21 cm observations from the SKA-Low to probe the primordial features predicted in inflation models. In particular, a class of inflation models based on particle physics predict bump-like feature(s) on the primordial power spectrum associated with a burst(s) of particle productions during inflation [9–12]. It was recently shown that such bursts of particle productions naturally occur in inflation models based on higher-dimensional gauge theories [13–15]. CMB data from *Planck* 2018 gives upper bounds on the amplitudes of bump-like features in the co-moving wave-number range $0.0002 \lesssim k(\text{Mpc}^{-1}) \lesssim 0.15$ [16]. In this work, we have investigated the possible constraints on the parameters of bump-like features using mock data of SKA-Low in the co-moving wave-number range $0.1 \lesssim k(\text{Mpc}^{-1}) \lesssim 1.0$. We focus on the scenario of a single burst of particle production that results in a single bump-like feature on the primordial power spectrum over this range of co-moving wave-numbers, parameterized by amplitude A_{I} and

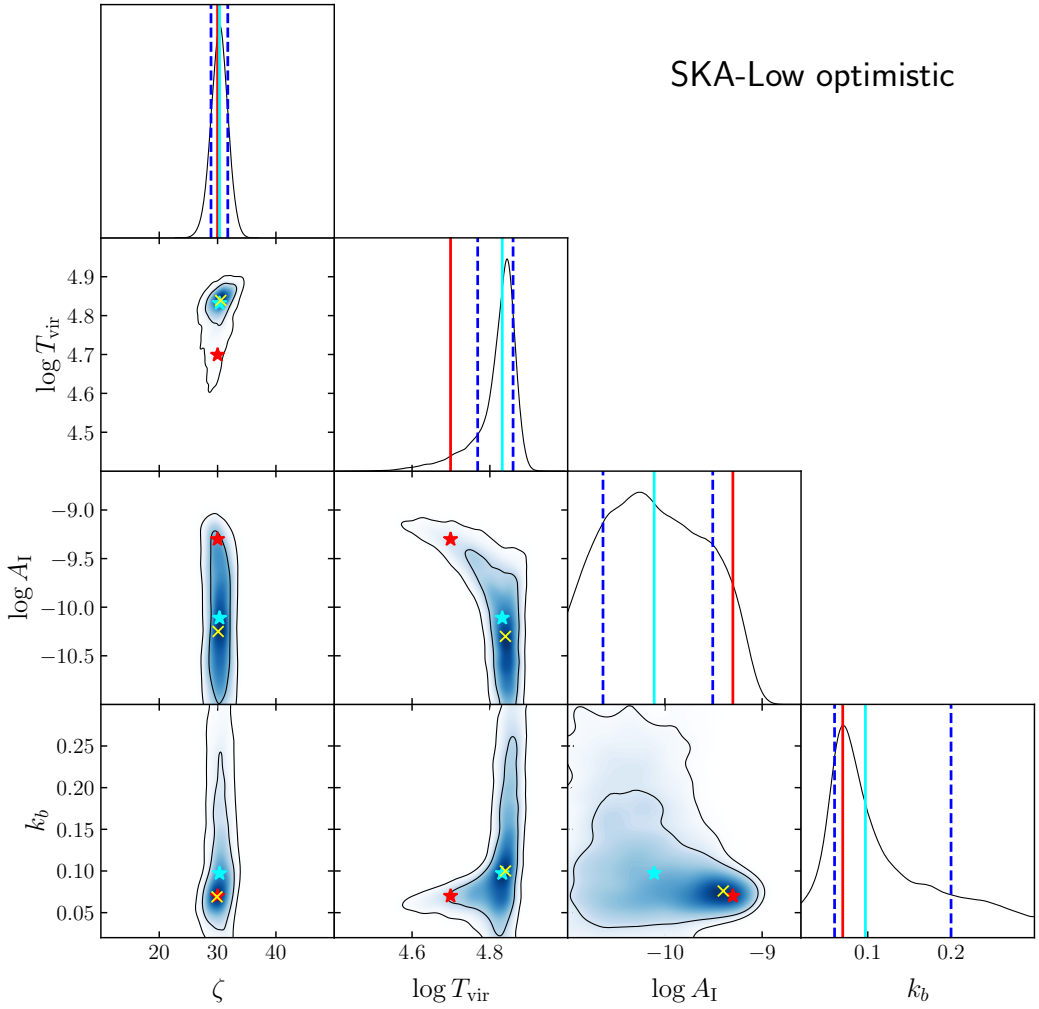


Figure 7: The posterior PDFs for the EoR and single bump model parameters: ζ , $\log T_{\text{vir}}$, $\log A_{\text{I}}$ and k_b . The two contours indicate the parameter space corresponding to 68% and 95% confidence levels. The red (cyan) star and lines mark the input parameter values (recovered median values from the SKA-Low) (table 3). The vertical dashed lines indicate 68% parameter space enclosed in the one-dimensional PDFs. The markers ‘ \times ’ denote maxima in each two-dimensional PDFs.

location $k_b(\text{Mpc}^{-1})$ via eq. (2.11). The mock 21 cm power spectra were created for the SKA-Low antenna configurations, and Bayesian analysis with MCMC sampling was performed to obtain posterior probability distribution on the parameters of interest.

We first studied a scenario in which we varied only those parameters relevant to the primordial features, i.e., A_{I} and k_b , and fixed all the astrophysical parameters to their fiducial values. We used both optimistic and moderate foreground removal models to estimate noise, and 20% modelling uncertainty was added to the noise power spectrum. Our results are summarized case by case as follows (see figure 6):

- Case I, input ($A_{\text{I}} = 10^{-9}, k_b = 0.1(\text{Mpc}^{-1})$): single bump parameters A_{I} and k_b were recovered within 68% CL of their input values. When the foreground removal model

was changed from optimistic to moderate case, the change in fractional uncertainties on the parameters was less than 0.1%.

- Case II, input ($A_I = 5 \times 10^{-10}$, $k_b = 0.07(\text{Mpc}^{-1})$): both the parameters were recovered within 68% CL of their input values. Compared with the optimistic case, the moderate foreground removal model increases the fractional errors on $\log A_I$ and k_b by 0.08% and 0.4%, respectively.
- Case III, input ($A_I = 5 \times 10^{-11}$, $k_b = 0.07(\text{Mpc}^{-1})$): both the parameters were recovered within 68% CL but with larger uncertainties. Compared to the previous case of a bump with an order of magnitude larger amplitude at the same location, the fractional errors on $\log A_I$ and k_b increased by 4% and 51%, respectively. Moreover, the recovered value of A_I shows mild bias towards the lower side, while that of k_b shows a relatively stronger bias towards the higher side.
- Case IV, input ($A_I = 3 \times 10^{-11}$, $k_b = 0.04(\text{Mpc}^{-1})$): a single bump model with the chosen parameters was allowed in the CMB data by *Planck* 2018 [16]. The results show that the location of the feature with such a small amplitude could be difficult to constrain from SKA-Low mock data. However, $\log A_I$ and k_b have recovered within 68% and 95% CL, respectively. The recovered value of k_b shows a stronger bias towards the higher side compared to Case III. This trend indicates that the location of the bump becomes harder to constrain as the input value of A_I is decreased. We note that the bias is observed when we compare the input values with the recovered *median* values in the cases when the shape of the one-dimensional PDF deviates strongly from the Gaussian form. We find that the maxima of the two-dimensional posterior PDFs are biased but still within 68% CL from the input parameter values.

In the next scenario, we attempted to simultaneously constrain astrophysical parameters along with the single bump model parameters. In principle, modelling the formation of the first stars, the heating of IGM, and the reionization of the universe involves many underlying astrophysical parameters. More unknown parameters make the parameter sampling computationally very expensive, particularly when the initial conditions need to be re-generated every time a new cosmological parameter is proposed. To perform the analysis in a reasonable computational time, we considered a simple model of EoR, in which we varied two of the astrophysical parameters: ionizing efficiency ζ and minimum virial temperature of star-forming halos T_{vir} (K). We add a modelling uncertainty of 20% to the noise power spectra in our analysis. The input parameters for creating mock power spectra are: $\zeta = 30$, $\log T_{\text{vir}} = 4.69897$, $A_I = 5 \times 10^{-10}$ and $k_b = 0.07(\text{Mpc}^{-1})$. We found that the parameters ζ and k_b have recovered within 68% CL, whereas $\log T_{\text{vir}}$ and $\log A_I$ have recovered within 95% CL. Compared with Case II (optimistic), we found that keeping ζ and $\log T_{\text{vir}}$ as free parameters increases the fractional errors on $\log A_I$ by 4% and k_b by 56%.

We note that particle production during inflation also leaves a bump-like feature on the bispectrum [12, 74]. Therefore, the bispectrum information from the future redshifted 21 cm signal may further constrain the primordial features discussed in this work. In the inflation models investigated here, multiple bursts of particle production can also occur during inflation, leading to a *multi-bump* or a series of bump-like features on the primordial power spectrum. Such models contain a parameter that quantifies the spacing between the bumps in addition to the amplitude and location of the first bump. As structure formation proceeds, it can be non-trivial to trace the signatures of different multi-bump models only using the

information from the two-point correlation functions. Therefore, joint analysis with higher-order correlators may be better suited to constrain the multi-bump models. We leave this case for future work.

The results presented in this work can be improved further if the estimated uncertainties are lowered, e.g., by increasing the observational hours or increasing the effective area of the telescope⁹. One can further reduce the modelling uncertainty by calibrating to more detailed radiative transfer simulations. There are other ways to characterize the redshifted 21 cm signal discussed in the literature (see [55] for an overview): apart from the mean of $\delta T_b(\vec{x})$ given by the global 21 cm signal, there are one-point statistics such as variance, skewness and kurtosis; geometrical and topological analysis of the 21 cm signal (see e. g. [76, 77]). Therefore, a joint analysis using various statistical measurements may be necessary to simultaneously constrain all the EoR and cosmological parameters, including that of primordial features. Such an analysis will be carried out in the future as an extension of this work. It is also expected that the combined analysis of redshifted 21 cm observations with future observations from other complementary probes, such as CMB polarization, large-scale structure surveys, and stochastic gravitational background waves, would provide the prospect of further constraining the inflation models.

Acknowledgements

SSN thanks the Indian Institute of Astrophysics, Bangalore, for the hospitality and support provided during an academic visit. The computational work in this paper was carried out using *Shakti*, a high-performance computing cluster at the Manipal Centre for Natural Sciences, Centre of Excellence, Manipal Academy of Higher Education.

This work was supported in part by Dr T.M.A. Pai Ph. D. scholarship program of Manipal Academy of Higher Education and the Science and Engineering Research Board, Department of Science and Technology, Government of India, under the project file number EMR/2015/002471.

A Degeneracy between the single bump model parameters and the EoR parameters

In this section, we discuss the degeneracy between the amplitude of the bump-like primordial features A_I and the parameters relevant for EoR (ζ, T_{vir}). As discussed in section 4.2, increasing ζ has similar effects on structure formation as decreasing T_{vir} and as increasing power on the primordial power spectrum by, e.g., adding a feature with amplitude A_I . In order to examine their correlation further, we consider how the following models differ from the fiducial one:

- **Model a:** increasing ζ from 30 (fiducial) to 50.
- **Model b:** decreasing T_{vir} from 5×10^4 (fiducial) to 3×10^4 .
- **Model c:** adding a bump-like primordial feature of amplitude 10^{-9} at $k_b = 0.05$.

The remaining parameters in the simulation are fixed to their benchmark values given in section 3.1. The corresponding ionization history encoded in the mean neutral fraction of

⁹E.g., the second phase of the SKA will have a larger collecting area than SKA1 [75].

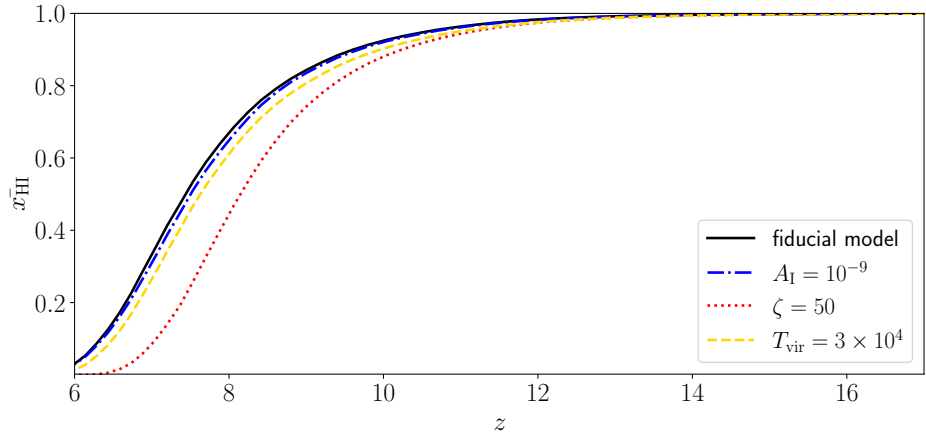


Figure 8: The average neutral fraction of hydrogen versus redshift z for the models under consideration.

hydrogen x_{HI} versus z for each model is shown in figure 8. We observe that introducing a bump feature quickens the ionization of the universe, similar to increasing ζ or decreasing T_{vir} . The figure, therefore, highlights the degeneracy between the three parameters in the ionization history.

To distinguish the models *a*, *b* and *c*, we next discuss their 21 cm power spectra. To quantify how each model differs from the fiducial one, we define the fractional difference of the power spectra, f_{21} , as

$$f_{21}(k) := \frac{\delta \Delta_{21}^2(k)}{\Delta_{21}^2(k)} = \frac{\Delta_{21}^2(k) - \Delta_{21}^{2,\text{fid}}(k)}{\Delta_{21}^{2,\text{fid}}(k)}, \quad (\text{A.1})$$

where the suffix ‘fid’ stands for the fiducial model. In figure 9, we plot Δ_{21}^2 (top panels) and f_{21} (lower panels) as functions of k at a few redshifts for all the models. We note the following points:

- The introduction of the bump enhances the power towards the lower k side (towards the location of the bump but not coincident), relative to the fiducial model, at all redshifts. This enhancement is distinct from the effects of varying ζ and T_{vir} , which are seen to (i) enhance power at all k at $z \sim 17$ and $z \sim 15$, (ii) enhance (suppress) at high (low) k values at $z \sim 13$ and $z \sim 12$, and (iii) suppress power at all k for $z \sim 10$ and $z \sim 7$.
- At relatively low redshifts ($z \sim 10$ and $z \sim 7$), the fractional difference drops down, and the bump model becomes hard to distinguish from the fiducial model, which demonstrates that the effect of the primordial bump-like feature is washed out towards the lower redshifts where the astrophysical details become very important. This is an important point to note when targeting to constrain primordial physics using the 21 cm power spectrum. In comparison, the different EoR models are quite distinct from the fiducial model.

In conclusion, we find that the 21 cm power spectrum for the bump model differs in shape and amplitude from the fiducial model, as well as from other models with different astrophysical parameter values. Moreover, the differences evolve with redshift. Therefore,

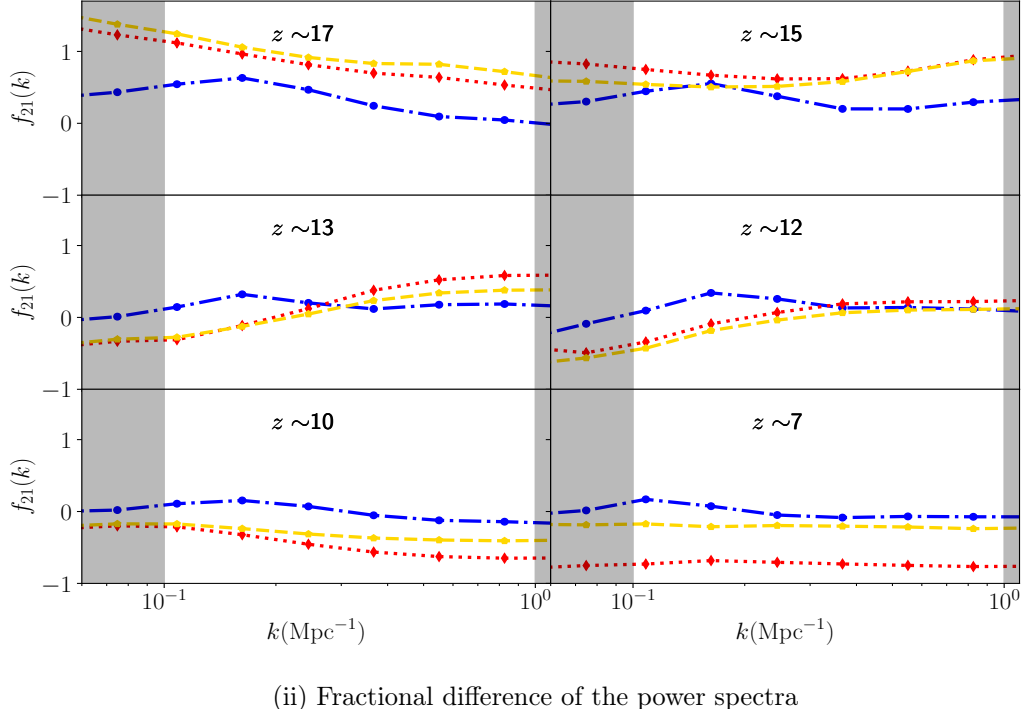
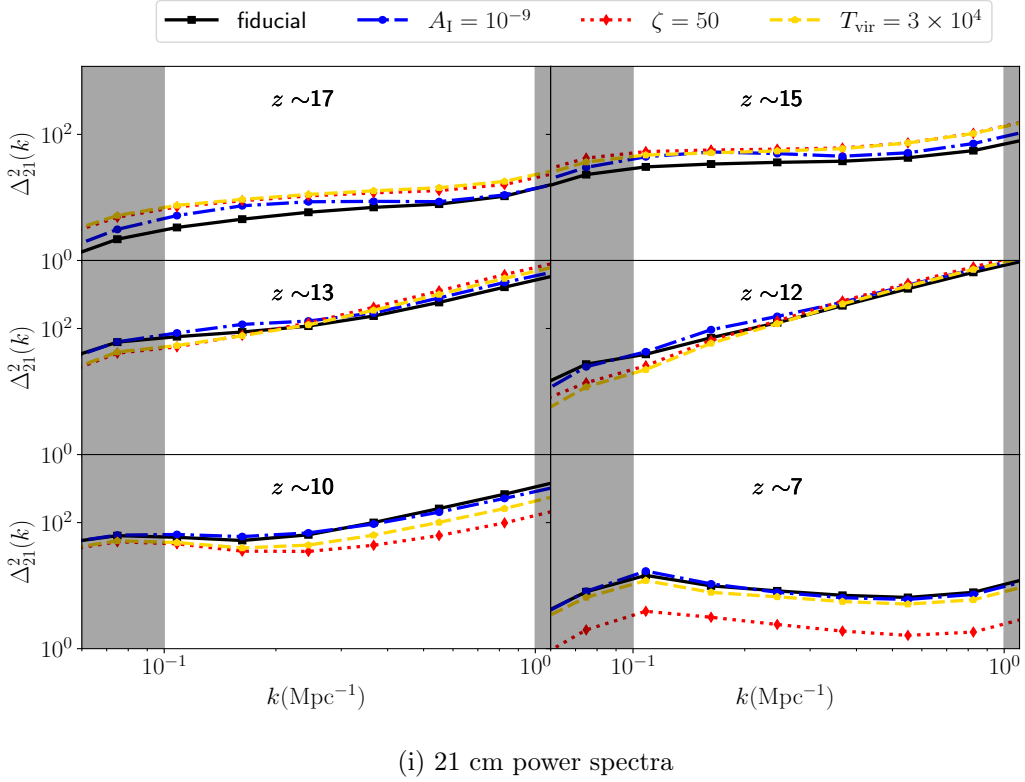


Figure 9: The simulated 21 cm power spectra for the fiducial model (featureless, $\zeta = 30$ and $T_{\text{vir}} = 5 \times 10^4$) are shown by blue solid lines. Models *a* (featureless, $\zeta = 50$), *b* (featureless, $T_{\text{vir}} = 3 \times 10^4$), and *c* (single bump with $A_I = 10^{-9}$, $k_b = 0.05$) are shown by dotted, dashed, and dot-dash lines, respectively. The simulated volume in 21cmFAST has a box length of 250 Mpc with 84^3 grids. The grey-shaded regions are excluded from our MCMC sampling.

the 21 cm power spectra measured across a wide range of wave-numbers and at multiple redshifts are necessary to break the degeneracy between the parameters of EoR and primordial feature. This is an encouraging finding from the point of view of using 21 cm observations to constrain primordial physics, such as particle production during inflation. However, the caveat is that observed data towards higher redshifts, where instrumental noise tends to increase, are required.

References

- [1] A.H. Guth, *Inflationary universe: A possible solution to the horizon and flatness problems*, *Phys. Rev. D* **23** (1981) 347.
- [2] A. Linde, *A new inflationary universe scenario: A possible solution of the horizon, flatness, homogeneity, isotropy and primordial monopole problems*, *Physics Letters B* **108** (1982) 389.
- [3] A. Albrecht and P.J. Steinhardt, *Cosmology for grand unified theories with radiatively induced symmetry breaking*, *Phys. Rev. Lett.* **48** (1982) 1220.
- [4] A. Starobinsky, *A new type of isotropic cosmological models without singularity*, *Physics Letters B* **91** (1980) 99.
- [5] K. Sato, *First-order phase transition of a vacuum and the expansion of the Universe*, *Monthly Notices of the Royal Astronomical Society* **195** (1981) 467 [<https://academic.oup.com/mnras/article-pdf/195/3/467/4065201/mnras195-0467.pdf>].
- [6] D. Kazanas, *Dynamics of the universe and spontaneous symmetry breaking*, *ApJ* **241** (1980) L59.
- [7] PLANCK collaboration, *Planck 2018 results. I. Overview and the cosmological legacy of Planck*, *Astron. Astrophys.* **641** (2020) A1 [[1807.06205](https://arxiv.org/abs/1807.06205)].
- [8] PLANCK collaboration, *Planck 2018 results. X. Constraints on inflation*, *Astron. Astrophys.* **641** (2020) A10 [[1807.06211](https://arxiv.org/abs/1807.06211)].
- [9] D.J.H. Chung, E.W. Kolb, A. Riotto and I.I. Tkachev, *Probing Planckian physics: Resonant production of particles during inflation and features in the primordial power spectrum*, *Phys. Rev. D* **62** (2000) 043508 [[hep-ph/9910437](https://arxiv.org/abs/hep-ph/9910437)].
- [10] N. Barnaby, Z. Huang, L. Kofman and D. Pogosyan, *Cosmological Fluctuations from Infra-Red Cascading During Inflation*, *Phys. Rev. D* **80** (2009) 043501 [[0902.0615](https://arxiv.org/abs/0902.0615)].
- [11] N. Barnaby and Z. Huang, *Particle Production During Inflation: Observational Constraints and Signatures*, *Phys. Rev. D* **80** (2009) 126018 [[0909.0751](https://arxiv.org/abs/0909.0751)].
- [12] L. Pearce, M. Peloso and L. Sorbo, *Resonant particle production during inflation: a full analytical study*, *JCAP* **1705** (2017) 054 [[1702.07661](https://arxiv.org/abs/1702.07661)].
- [13] K. Furuuchi, *Excursions through KK modes*, *JCAP* **1607** (2016) 008 [[1512.04684](https://arxiv.org/abs/1512.04684)].
- [14] K. Furuuchi, S.S. Naik and N.J. Jobu, *Large Field Excursions from Dimensional (De)construction*, *JCAP* **06** (2020) 054 [[2001.06518](https://arxiv.org/abs/2001.06518)].
- [15] K. Furuuchi, N.J. Jobu and S.S. Naik, *Extra-Natural Inflation (De)constructed*, [2004.13755](https://arxiv.org/abs/2004.13755).
- [16] S.S. Naik, K. Furuuchi and P. Chingangbam, *Particle production during inflation: a Bayesian analysis with CMB data from Planck 2018*, *JCAP* **07** (2022) 016 [[2202.05862](https://arxiv.org/abs/2202.05862)].
- [17] M. Ballardini, F. Finelli, F. Marulli, L. Moscardini and A. Veropalumbo, *New constraints on primordial features from the galaxy two-point correlation function*, [2202.08819](https://arxiv.org/abs/2202.08819).
- [18] D. Chandra and S. Pal, *Investigating the constraints on primordial features with future cosmic microwave background and galaxy surveys*, *JCAP* **09** (2022) 024 [[2205.01164](https://arxiv.org/abs/2205.01164)].

[19] S. Furlanetto, S.P. Oh and F. Briggs, *Cosmology at Low Frequencies: The 21 cm Transition and the High-Redshift Universe*, *Phys. Rept.* **433** (2006) 181 [[astro-ph/0608032](#)].

[20] S.R. Furlanetto, A. Lidz, A. Loeb, M. McQuinn, J.R. Pritchard, P.R. Shapiro et al., *Cosmology from the Highly-Redshifted 21 cm Line*, in *astro2010: The Astronomy and Astrophysics Decadal Survey*, vol. 2010, p. 82, Jan., 2009 [[0902.3259](#)].

[21] J.R. Pritchard and A. Loeb, *21 cm cosmology in the 21st century*, *Reports on Progress in Physics* **75** (2012) 086901 [[1109.6012](#)].

[22] A. Loeb and M. Zaldarriaga, *Measuring the small - scale power spectrum of cosmic density fluctuations through 21 cm tomography prior to the epoch of structure formation*, *Phys. Rev. Lett.* **92** (2004) 211301 [[astro-ph/0312134](#)].

[23] <https://reionization.org/>.

[24] <http://www.skatelescope.org/>.

[25] X. Chen, P.D. Meerburg and M. Münchmeyer, *The Future of Primordial Features with 21 cm Tomography*, *JCAP* **09** (2016) 023 [[1605.09364](#)].

[26] Y. Xu, J. Hamann and X. Chen, *Precise measurements of inflationary features with 21 cm observations*, *Phys. Rev. D* **94** (2016) 123518 [[1607.00817](#)].

[27] SKA collaboration, *Cosmology with Phase 1 of the Square Kilometre Array: Red Book 2018: Technical specifications and performance forecasts*, *Publ. Astron. Soc. Austral.* **37** (2020) e007 [[1811.02743](#)].

[28] <http://tianlai.bao.ac.cn/>.

[29] M. Ballardini, F. Finelli, R. Maartens and L. Moscardini, *Probing primordial features with next-generation photometric and radio surveys*, *JCAP* **04** (2018) 044 [[1712.07425](#)].

[30] <https://www.lsst.org/>.

[31] J.D. Bowman, A.E.E. Rogers, R.A. Monsalve, T.J. Mozdzen and N. Mahesh, *An absorption profile centred at 78 megahertz in the sky-averaged spectrum*, *Nature* **555** (2018) 67 [[1810.05912](#)].

[32] S. Yoshiura, K. Takahashi and T. Takahashi, *Impact of EDGES 21-cm global signal on the primordial power spectrum*, *Phys. Rev. D* **98** (2018) 063529 [[1805.11806](#)].

[33] S. Yoshiura, K. Takahashi and T. Takahashi, *Probing Small Scale Primordial Power Spectrum with 21cm Line Global Signal*, *Phys. Rev. D* **101** (2020) 083520 [[1911.07442](#)].

[34] A. Mesinger, *The Cosmic 21-cm Revolution; Charting the first billion years of our universe* (2019), [10.1088/2514-3433/ab4a73](#).

[35] P. Madau, A. Meiksin and M.J. Rees, *21-CM tomography of the intergalactic medium at high redshift*, *Astrophys. J.* **475** (1997) 429 [[astro-ph/9608010](#)].

[36] R. Barkana and A. Loeb, *In the beginning: The First sources of light and the reionization of the Universe*, *Phys. Rept.* **349** (2001) 125 [[astro-ph/0010468](#)].

[37] A. Mesinger, S. Furlanetto and R. Cen, *21CMFAST: a fast, seminumerical simulation of the high-redshift 21-cm signal*, *Mon. Not. Roy. Astron. Soc.* **411** (2011) 955 [[1003.3878](#)].

[38] <https://github.com/andreimesinger/21cmFAST>.

[39] J. Park, A. Mesinger, B. Greig and N. Gillet, *Inferring the astrophysics of reionization and cosmic dawn from galaxy luminosity functions and the 21-cm signal*, *Mon. Not. Roy. Astron. Soc.* **484** (2019) 933 [[1809.08995](#)].

[40] D.J. Eisenstein and W. Hu, *Baryonic features in the matter transfer function*, *Astrophys. J.* **496** (1998) 605 [[astro-ph/9709112](#)].

[41] D.J. Eisenstein and W. Hu, *Power spectra for cold dark matter and its variants*, *Astrophys. J.* **511** (1997) 5 [[astro-ph/9710252](#)].

[42] H.D. Kaur, N. Gillet and A. Mesinger, *Minimum size of 21-cm simulations*, *Monthly Notices of the Royal Astronomical Society* **495** (2020) 2354 [<https://academic.oup.com/mnras/article-pdf/495/2/2354/33323159/staa1323.pdf>].

[43] J.C. Pober, A.R. Parsons, D.R. DeBoer, P. McDonald, M. McQuinn, J.E. Aguirre et al., *The Baryon Acoustic Oscillation Broadband and Broad-beam Array: Design Overview and Sensitivity Forecasts*, *AJ* **145** (2013) 65 [[1210.2413](#)].

[44] J.C. Pober et al., *What Next-Generation 21 cm Power Spectrum Measurements Can Teach Us About the Epoch of Reionization*, *Astrophys. J.* **782** (2014) 66 [[1310.7031](#)].

[45] <https://github.com/jpober/21cmSense>.

[46] https://astronomers.skatelescope.org/wp-content/uploads/2016/09/SKA-TEL-SK0-0000422_02_SKA1_LowConfigurationCoordinates-1.pdf.

[47] A. Parsons, J. Pober, M. McQuinn, D. Jacobs and J. Aguirre, *A sensitivity and array-configuration study for measuring the power spectrum of 21 cm emission from reionization*, *The Astrophysical Journal* **753** (2012) 81.

[48] A.R. Thompson, J.M. Moran and J. Swenson, George W., *Interferometry and Synthesis in Radio Astronomy, 2nd Edition* (2001).

[49] B. Greig and A. Mesinger, *21CMMC: an MCMC analysis tool enabling astrophysical parameter studies of the cosmic 21 cm signal*, *Mon. Not. Roy. Astron. Soc.* **449** (2015) 4246 [[1501.06576](#)].

[50] B. Greig and A. Mesinger, *Simultaneously constraining the astrophysics of reionization and the epoch of heating with 21CMMC*, *Mon. Not. Roy. Astron. Soc.* **472** (2017) 2651 [[1705.03471](#)].

[51] <https://github.com/BradGreig/21CMMC>.

[52] D. Foreman-Mackey, D.W. Hogg, D. Lang and J. Goodman, *emcee: The MCMC Hammer*, *PASP* **125** (2013) 306 [[1202.3665](#)].

[53] S. Singh, N.T. Jishnu, R. Subrahmanyam, N. Udaya Shankar, B.S. Girish, A. Raghunathan et al., *On the detection of a cosmic dawn signal in the radio background*, *Nature Astronomy* **6** (2022) 607 [[2112.06778](#)].

[54] G. Paciga et al., *A refined foreground-corrected limit on the HI power spectrum at $z=8.6$ from the GMRT Epoch of Reionization Experiment*, *Mon. Not. Roy. Astron. Soc.* **433** (2013) 639 [[1301.5906](#)].

[55] F.G. Mertens et al., *Improved upper limits on the 21-cm signal power spectrum of neutral hydrogen at $z \approx 9.1$ from LOFAR*, *Mon. Not. Roy. Astron. Soc.* **493** (2020) 1662 [[2002.07196](#)].

[56] A.H. Patil et al., *Upper limits on the 21-cm Epoch of Reionization power spectrum from one night with LOFAR*, *Astrophys. J.* **838** (2017) 65 [[1702.08679](#)].

[57] B.K. Gehlot, F.G. Mertens, L.V.E. Koopmans, M.A. Brentjens, S. Zaroubi, B. Ciardi et al., *The first power spectrum limit on the 21-cm signal of neutral hydrogen during the Cosmic Dawn at $z = 20-25$ from LOFAR*, *MNRAS* **488** (2019) 4271 [[1809.06661](#)].

[58] J.S. Dillon et al., *Overcoming real-world obstacles in 21 cm power spectrum estimation: A method demonstration and results from early Murchison Widefield Array data*, *Phys. Rev. D* **89** (2014) 023002 [[1304.4229](#)].

[59] N. Barry, M. Wilensky, C.M. Trott, B. Pindor, A.P. Beardsley, B.J. Hazelton et al., *Improving the Epoch of Reionization Power Spectrum Results from Murchison Widefield Array Season 1 Observations*, *ApJ* **884** (2019) 1 [[1909.00561](#)].

[60] A.P. Beardsley, B.J. Hazelton, I.S. Sullivan, P. Carroll, N. Barry, M. Rahimi et al., *First Season MWA EoR Power spectrum Results at Redshift 7*, *ApJ* **833** (2016) 102 [[1608.06281](#)].

[61] J.S. Dillon et al., *Empirical Covariance Modeling for 21 cm Power Spectrum Estimation: A Method Demonstration and New Limits from Early Murchison Widefield Array 128-Tile Data*, *Phys. Rev. D* **91** (2015) 123011 [[1506.01026](#)].

[62] A. Ewall-Wice et al., *First limits on the 21 cm power spectrum during the Epoch of X-ray heating*, *Mon. Not. Roy. Astron. Soc.* **460** (2016) 4320 [[1605.00016](#)].

[63] C.M. Trott et al., *Deep multiredshift limits on Epoch of Reionization 21 cm power spectra from four seasons of Murchison Widefield Array observations*, *Mon. Not. Roy. Astron. Soc.* **493** (2020) 4711 [[2002.02575](#)].

[64] S. Yoshiura et al., *A new MWA limit on the 21 cm power spectrum at redshifts $\sim 13\text{--}17$* , *Mon. Not. Roy. Astron. Soc.* **505** (2021) 4775 [[2105.12888](#)].

[65] W. Li, J.C. Pober, N. Barry, B.J. Hazelton, M.F. Morales, C.M. Trott et al., *First Season MWA Phase II Epoch of Reionization Power Spectrum Results at Redshift 7*, *ApJ* **887** (2019) 141 [[1911.10216](#)].

[66] A.K. Patwa, S. Sethi and K.S. Dwarakanath, *Extracting the 21 cm EoR signal using MWA drift scan data*, *Mon. Not. Roy. Astron. Soc.* **504** (2021) 2062 [[2104.03321](#)].

[67] M. Kolopanis, D.C. Jacobs, C. Cheng, A.R. Parsons, S.A. Kohn, J.C. Pober et al., *A Simplified, Lossless Reanalysis of PAPER-64*, *ApJ* **883** (2019) 133 [[1909.02085](#)].

[68] M.W. Eastwood et al., *The 21 cm Power Spectrum from the Cosmic Dawn: First Results from the OVRO-LWA*, *Astron. J.* **158** (2019) 84 [[1906.08943](#)].

[69] H. Garsden, L. Greenhill, G. Bernardi, A. Fialkov, D.C. Price, D. Mitchell et al., *A 21-cm power spectrum at 48 MHz, using the Owens Valley Long Wavelength Array*, *Mon. Not. Roy. Astron. Soc.* **506** (2021) 5802 [[2102.09596](#)].

[70] B.K. Gehlot et al., *The AARTFAAC Cosmic Explorer: observations of the 21-cm power spectrum in the EDGES absorption trough*, *Mon. Not. Roy. Astron. Soc.* **499** (2020) 4158 [[2010.02269](#)].

[71] HERA collaboration, *First Results from HERA Phase I: Upper Limits on the Epoch of Reionization 21 cm Power Spectrum*, *Astrophys. J.* **925** (2022) 221 [[2108.02263](#)].

[72] HERA collaboration, *Improved Constraints on the 21 cm EoR Power Spectrum and the X-Ray Heating of the IGM with HERA Phase I Observations*, [2210.04912](#).

[73] A. Lewis, *GetDist: a Python package for analysing Monte Carlo samples*, [1910.13970](#).

[74] N. Barnaby, *Nongaussianity from Particle Production During Inflation*, *Adv. Astron.* **2010** (2010) 156180 [[1010.5507](#)].

[75] A. Weltman et al., *Fundamental physics with the Square Kilometre Array*, *Publ. Astron. Soc. Austral.* **37** (2020) e002 [[1810.02680](#)].

[76] A. Kapahtia, P. Chingangbam, S. Appleby and C. Park, *A novel probe of ionized bubble shape and size statistics of the epoch of reionization using the contour Minkowski Tensor*, *JCAP* **10** (2018) 011 [[1712.09195](#)].

[77] A. Kapahtia, P. Chingangbam, R. Ghara, S. Appleby and T.R. Choudhury, *Prospects of constraining reionization model parameters using Minkowski tensors and Betti numbers*, *JCAP* **05** (2021) 026 [[2101.03962](#)].